Simulations of the fault current limiting operation of a long-length REBCO CORC® superconducting cable cooled by helium gas

Linh Ngoc Nguyen[1] ⓘ**, Do Vo**[1]**, Jeremy Weiss**[2,3] ⓘ**, Sven A Dönges**[3]**, Francesco Grilli**[4] ⓘ**, Danko van der Laan**[2,3] ⓘ**, Sastry V Pamidi**[5] **and Doan Ngoc Nguyen**[1,*] ⓘ

[1] Los Alamos National Laboratory, Los Alamos, NM 87544, United States of America
[2] University of Colorado, Boulder, CO 80301, United States of America
[3] Advanced Conductor Technologies, LLC, Boulder, CO 80301, United States of America
[4] Institute for Technical Physics, Karlsruhe Institute of Technology, Karlsruhe, Germany
[5] Center for Advanced Power Systems, FAMU-FSU College of Engineering, Tallahassee, FL 32310, United States of America

E-mail: doan@lanl.gov

CrossMark

Abstract

Conductor-on-round-core (CORC®) cables composed of rare-earth-barium-copper-oxide high-temperature superconducting (HTS) tapes are of great interest for power transmission applications due to their many advantages such as high power density, light weight, and low loss. Closed circulation loops of cryogenic helium gas can be used to cool HTS cables down to low temperatures to significantly improve their current-carrying capacity. Coupled circuit-electromagnetic-thermal finite element simulations implemented in the COMSOL Multiphysics package were developed, validated, and then used for simulating the fault current limiting (FCL) performance and the cooling processes of an 8-layer CORC® cable cooled with a flow of cryogenic helium gas. In the simulations, the temperature dependence of the electrical and thermal properties of all component materials is implemented for improved accuracy. To overcome computational challenges caused by the considerable difference in geometrical scales (i.e. few-μm-thick HTS layers versus 10 m-long HTS cable), the model is divided into two separate simulations. The first simulation is performed on the transverse cross-section of the cable to calculate the electric field, heating power and temperature rise in each component of a CORC® cable during FCL operation. The heating power calculated in the first simulation is transferred to the second model to simulate the cooling of a 10 m-long cable after the fault is cleared. The effect of the helium gas flow rate on the cooling process is also investigated to develop strategic approaches for optimizing cooling systems for HTS cables with FCL capability. The simulations indicated that a 40 ms fault with a voltage drop of 20 V m^{-1}

---

[*] Author to whom any correspondence should be addressed.

along the cable can result in a temperature increase from 60 K to about 165 K inside the cable, and it takes about 500 s to cool the cable back to nearly 60 K with a flow of cold helium gas at a rate of 5 g s^{-1}.

1. Introduction

High-temperature superconducting (HTS) power cables offer an attractive option for replacing conventional metal conductors in power transmission and distribution [1–4]. These cables offer several significant advantages, including higher power density, reduced size, and lower weight. Additionally, the rapid transition from the superconducting to the normal state in HTS cables when the current exceeds the critical current (I_c) is utilized to suppress current surges caused by faults in the power grid, thereby enabling more resilient power transmission and distribution systems. Extensive research and development efforts have focused on assessing and improving the fault current limiting (FCL) capabilities of HTS power cables through design advancements [5–7].

HTS cables commonly operate at 65–77 K using low-cost, abundantly available liquid nitrogen as a coolant using subcooled and pressurized systems [8–10]. The critical current of the HTS cables (and therefore the operating current) will increase substantially when they are cooled by cryogenic helium gas to operate at lower temperatures [6, 11]. The HTS power transmission cables cooled by a closed loop of cryogenic helium gas are particularly beneficial for electric ships and aircraft due to the mobility and exceptionally high power density these systems provide [11, 12].

In practical applications, when a fault occurs, an HTS cable quickly responds to limit the fault current to a level that enables traditional protection systems to safely interrupt the fault. This process typically takes several tens of milliseconds (a fraction of a power cycle), depending on the response time of the breakers. During the brief fault period, the HTS cable carries an electrical current significantly higher than its critical current I_c. As a result, a substantial amount of heat is generated within the cable, causing the temperatures of its components to rise rapidly. The temperature of the HTS tapes inside the cable will exceed the critical temperature T_c, at which point all the fault current will be carried by the metal layers until the fault is cleared. Once the fault is cleared, cooling must be applied to the cable to dissipate the heat and return it to its normal operating temperature, allowing for re-energization.

This paper leverages advanced coupling of circuit, electromagnetic, thermal, and fluid dynamic finite element (FE) models implemented in the COMSOL Multiphysics package to provide comprehensive models for predicting the FCL performance and cooling processes of advanced HTS cable systems. Section 2 presents the description and key improvements made to the 2D transverse cross-section model for simulating cable FCL performance. Section 3 offers a brief

overview of fault current experiments and the validation of the enhanced 2D transverse model. In section 4, a new numerical model is introduced to predict the critical current of rare-earth-barium-copper-oxide (REBCO) conductor-on-round-core (CORC®) cable at various temperatures, along with its validation. Section 5 presents simulations of the FCL performance of the cable operating at 60 K in helium gas, achieved by coupling the circuit model with the validated 2D transverse model. Finally, section 6 addresses simulations of post-fault cooling for a 10 m-long REBCO CORC® cable operating at 60 K under varying coolant flow rates.

It is worth mentioning that all the above studies were performed on only one CORC® cable sample but under different operating conditions. The cable sample has 8 layers with 3 HTS tapes per layer, wound on an aluminum core which is electrically insulated from the HTS layers. Therefore, the core does not carry any electrical current, but it was considered in thermal transfer simulation. The properties of the CORC® cable are listed in table 1 and figure 1 illustrates a cross section of the cable.

2. The 2D transverse model for FCL performance

We recently reported the development and validation of a 2D transverse model to simulate the FCL performance of 8-layer CORC® HTS cables with different core materials [13]. This is a coupled thermal-electromagnetic finite element method (FEM) model implemented in the COMSOL Multiphysics package and performed in the 2D transverse cross-section of the cable. The electrical model is based on the common *H*-formulation [14] to calculate the evolution of the current distribution and the ohmic heating in the cable during a fault. The governing equations of this model include [14]:

$$\boldsymbol{J} = \nabla \times \boldsymbol{H} \tag{1}$$

$$\nabla \times \rho \nabla \times \boldsymbol{H} = -\mu \frac{\partial \boldsymbol{H}}{\partial t}. \tag{2}$$

The resistivity of superconducting layer follows the well-known power law:

$$\boldsymbol{E} = E_0 \left(\frac{\boldsymbol{J}}{J_c(T)} \right)^n \tag{3}$$

where $E_0 = 0.0001$ V m^{-1} and $J_c(T)$ is the critical current density of the superconducting layers, which is calculated from the value of the cable critical current $I_c(T)$.

Table 1. Properties of REBCO CORC® cable.

Parameters	Values
Core material	Aluminum
Number of layers	8
Number of tapes per layer	3
Former diameter (mm)	4.95
Outer diameter (mm)	7.18
I_c at 76 K (A)	2930
HTS tape width (mm)	4.02
HTS thickness (μm)	1.8
Substrate thickness (μm)	50
Copper thickness (stabilizer) (μm)	5
Silver thickness (stabilizer) (μm)	1.5
Thickness of Kapton layer (mm)	4.7
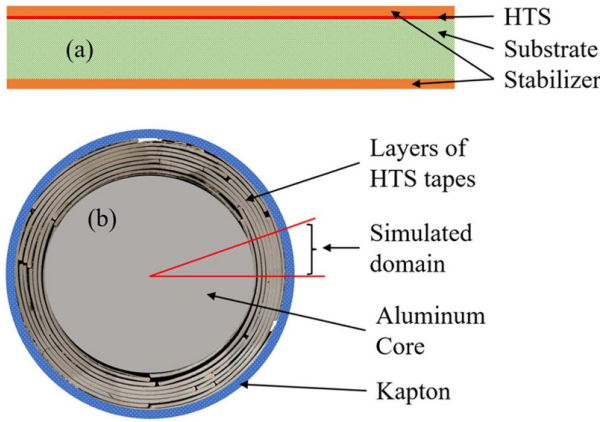
Figure 1. Cross section of typical REBCO tape and CORC® cable.

Determination of the cable critical current $I_c(T)$, based on the typical field dependence of the critical current density $J_c(B, T)$ for REBCO tapes, is given in detail in section 4.

While the model reproduces the experimental data well for a cable with a copper core, a 15% discrepancy was observed between the simulated and experimental results for a cable with a stainless-steel core. In the stainless-steel core cable, most of the current exceeding the cable's I_c is carried by the thin copper and silver layers of the HTS tapes. As a result, a significant amount of Ohmic heat is generated in the cable within a very brief period, making thermal transfer simulations more challenging and highly sensitive to cable parameters. While the model accounted for the spiral winding of HTS tape by using the effective length of the HTS tapes in the cable [13], the electrical contacts between the HTS layers were not considered. To incorporate these electrical contacts into the simulations, a 3D model would typically be required. However, a 3D model using *H*-formulation for an 8-layer cable is extremely complex and may not be necessary for FCL simulations. In this paper, a new, simpler approach is introduced by using the effective thicknesses of the Cu and Ag layers to account for electrical contact in the 2D transverse model,

thereby improving accuracy. The effective thicknesses were determined from measured cable resistances across a wide temperature range above the critical temperature T_c of YBCO tapes. When the temperature is above the critical temperature of YBCO tapes, the current in the cable is only carried by the substrate, Cu and Ag layers of YBCO tapes. Assuming that YBCO tapes are uniform along the cable, then there would be no current sharing between the tapes in the same layer and the copper, silver, and substrate layers are connected in parallel. Thus, the resistance of a cable with n layers and m tapes in each layer can be calculated as

$$\frac{1}{R_{\text{cable}}} = \sum_{i=1}^{n} \sum_{j=1}^{m} \frac{1}{R_{i,j}^{\text{sub}}} + \frac{1}{R_{i,j}^{\text{Cu}}} + \frac{1}{R_{i,j}^{\text{Ag}}}, \tag{4}$$

where R_{cable} is the cable resistance and $R_{i,j}^{\text{Cu}}, R_{i,j}^{\text{Ag}}$ and $R_{i,j}^{\text{Sub}}$ are the resistances of copper, silver and substrate domains of the *j*th tape on the *i*th layer, respectively. The resistances of substrate, Cu and Ag layers ($R_{i,j}^{\text{Cu}}, R_{i,j}^{\text{Ag}}$ and $R_{i,j}^{\text{Sub}}$) can be easily calculated from their geometric parameters (thickness, width and length) and their temperature dependent resistivities. Thus, equation (4) can be used to calculate the cable resistance at any temperature above the T_c.

Due to the significantly higher resistivity of the Hastelloy substrate compared to Cu and Ag (especially at cryogenic temperatures) and its minimal temperature dependence, the variation in cable resistance with temperature primarily arises from the Cu and Ag layers. In principle, layer-to-layer contact is not considered in equation (4) for analytically calculating cable resistance. However, this contact can generally be accounted for by using the 'effective' thicknesses (rather than the actual thicknesses) of the Cu and Ag layers in equation (4). Therefore, to determine the effective thicknesses of Cu and Ag layers, they were slightly varied about their nominal values provided by the tape manufacturer, so that the cable resistances calculated by equation (4) best reproduce the measured cable resistance for a wide range of temperatures (the thickness of the substrate is kept constant and equal to 50 μm for the HTS tapes used for the cable). Figure 2 plots the experimental data for cable resistances when the temperature increases from 77 K to 200 K. The cable resistance as a function of temperature between 100 K to 200 K calculated by equation (4) for several sets of the thicknesses of Cu and Ag layers was also plotted for comparison. Clearly, the cable resistance calculated with manufacture values of the thicknesses of Cu and Ag layers ($t_{\text{Ag}} = 1.5$ μm and $t_{\text{Cu}} = 5$ μm) is quite lower than the experimental data. The optimal match between the experimental cable resistance and the analytical cable resistance was obtained with the effective thicknesses of 4.1 μm for the Cu layer and 1 μm for the Ag layer. The effective thickness of the Cu layer is slightly thinner than the actual thickness specified by the HTS tape manufacturer. That difference indicates that there is an electrical current crossing the layers though their contact surface during measuring cable resistance at temperature $T > T_c$ and 2D analytical model using equation (4) to calculate the cable resistance must use effective thicknesses of Cu
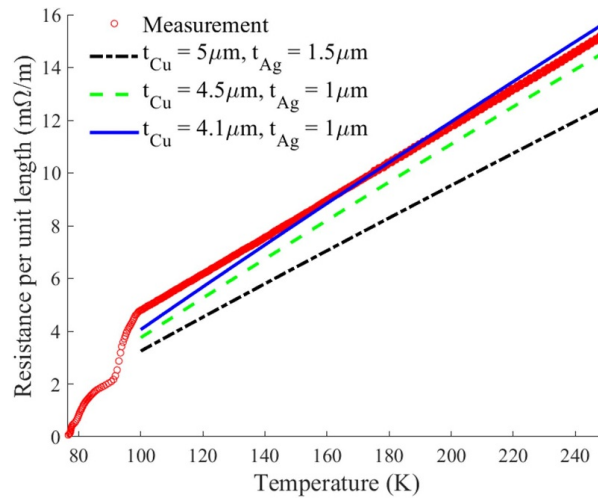
Figure 2. The cable resistance as a function of temperature between 100 K–200 K calculated by equation (4) for several sets of the thicknesses of Cu and Ag layers is plotted to compare with the experimental data.
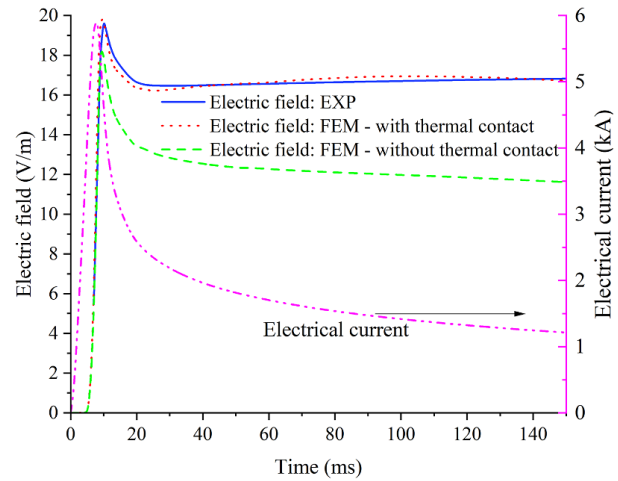

Figure 3. The electric fields and electrical current in the cable during a 150 ms fault for which the transport current surges to about nearly twice the cable critical current.

and Ag layers to account for the layer-to-layer electrical contact and thus achieve better agreement with the experimental data. Therefore, the effective thickness of Cu and Ag layers also need to be used in the 2D FEM FCL simulations for better accuracy.

The thermal contact resistance between REBCO tapes in the two adjacent layers may also play an important role in the heat transfer inside the CORC® cable. Therefore, in addition to implementing the effective thickness of the Cu and Ag layers, the 2D transverse model was further improved by including the thermal contact resistance, R_s, between the HTS layers in the thermal transfer simulation. The impact of thermal contact resistance in cable winding on their quench behavior has been investigated elsewhere [15, 16]. This thermal contact resistance changes slowly with contact pressure [17, 18]. However, the variation in winding pressure due to the varying cable temperature is not significant enough to warrant its consideration. In fact, our improved 2D transverse model only needs to use a constant thermal resistance for copper-copper contact, $R_s = 9 \times 10^{-5}$ K m^2 W^{-1} [17] to produce results that align well with experimental data for the entire 150 ms fault duration, as discussed in more detail in section 3.

3. Fault current experiment and validation of the improved FEM transverse model

The improved simulated model was validated against the overcurrent experiments on the CORC® cable sample with specifications listed in table 1. In the fault current tests at 76 K, the current was ramped up at 1 MA s^{-1} until the electric field along the cable reached approximately 20 V m^{-1}. The voltage

drop was then intended to be kept at that level for approximately 150 ms to assess the capability of the cable to withstand the heat load and to limit the current in the circuit, as seen in figure 3. Due to the heating in current leads connecting the power supply to the HTS cable during the current surge, the circuit resistance somewhat increased. The power supply reacted to that resistance increase, causing a slight drop of the electric field to a nearly flat level of 17 V m^{-1} after briefly reaching 20 V m^{-1} as preset. The fault current surged to 5800 kA, or about 200% of cable I_c, then quickly dropped to the lowest value of 1.2 kA at $t = 150$ ms, thanks to the current limiting capability of the HTS cable.

The 2D transverse model used the measured cable current pulse as the input to calculate the temperature rise, the current sharing between the constituent layers (HTS layers, substrate, Cu and Ag layers) and the voltage drop to validate against the experimental data. To compare with the experimental data, figure 3 also shows the voltage drops along the cable calculated both with and without accounting for the thermal contact resistance. When the thermal contact resistance was not considered, the simulated voltage drop is up to 20% lower than the experimentally observed results. However, when the thermal contact resistance was considered, the simulation reproduces the experimental data well for the entire length of the over current pulse. The good agreement between simulated and experimental results for the entire length of the 150 ms fault confirms the remarkable improvement in the accuracy of our model.

The model was also used to calculate the temperature evolution inside the cable during the pulse. Figure 4 shows that, at $t = 150$ ms, the cable temperature rose to 240 K when thermal contact resistance between the HTS tapes was considered and to 170 K when thermal contact resistance was not included in the simulation. When thermal contact resistance is taken into account, heat is retained in the HTS tapes for a longer
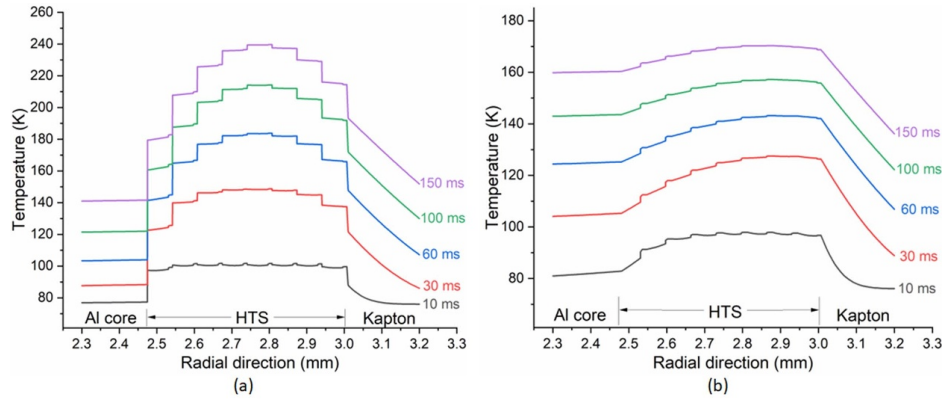
Figure 4. Evolution of temperature along the radial direction with respect to time: (a) with thermal contact resistance among REBCO tapes; (b) without thermal contact resistance among REBCO tapes.

period, leading to a higher temperature rise inside the cable. Comparisons of the results obtained with and without considering thermal contact resistance, shown in figures 3 and 4, indicate that thermal contact resistance plays a significant role in the thermal transfer process during a fault and should be considered for accurate simulation of the FCL performance of REBCO CORC® cables. This is especially important for the cable studied in this paper, which has an electrically isolated metal core. Since no current flows through the core, all the fault current is carried by the stabilizer layers, with the HTS layers becoming non-conductive as their temperature exceeds the critical temperature T_c. As a result, the temperature rise—and consequently, the voltage drop—are highly sensitive to the thermal transfer process inside the cable. For improved accuracy, the effective thicknesses of the Cu and Ag layers along with the thermal contact resistance $R_s = 9 \times 10^{-5}$ Km^2 W^{-1}, have been incorporated into all the simulation models.

Figure 5 illustrates in more detail the temporal behavior of the current through different components of the cable, including the aluminum core, substrate, stabilizer, and HTS layers, during a fault current event. The total current computed in the cable is obtained by summing the currents of each individual component. As seen in figure 5, the computed total current in the cable coincides with the experimental data. The current pulse has a peak current of about 5900 A, about 3000 A higher than cable I_c at 76 K. As anticipated, the HTS layers carry all the current when it is lower than the cable I_c. As the total current surpasses I_c (76 K) at approximately $t = 4$ ms, it begins distributing to the other components. Because the core is electrically isolated, it does not carry any current. With much higher electrical conductivity, the stabilizer layers of the HTS tapes carry a significant fraction of the current even though those layers are only about 5.1 μm thick (summation of computed thicknesses of copper and silver layers). Consequently, the temperature in the HTS tapes increases quickly, resulting in a fast drop in the current density in the HTS layers. At $t = 8$ ms, the current density in the HTS layers effectively vanishes, indicating that the temperature in the HTS layers is above T_c. After 8 ms, most of the current is carried by the stabilizer layers. The electrical currents carried in the substrate
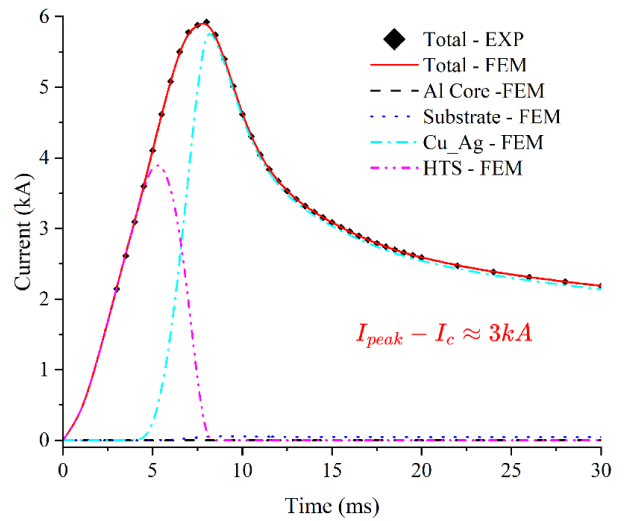

Figure 5. Electrical currents in different cable components during a fault for which the transport current surges to about twice the cable critical current.

layers are considerably low compared to those carried in the stabilizers for the entire duration of the pulse, because of the high electrical resistance of the Hastelloy.

4. Prediction of critical current of REBCO CORC® cable at different temperature

To accurately predict the FCL performance of the HTS cable at lower temperatures, the temperature dependence of the critical current of the cable must be known. In this section, we propose a simple numerical approach to determine the critical current of the CORC® cable at different temperatures. In this method, the temperature dependence of the critical current of a single tape published by Wimbush *et al* was used [19]. Because our sample cable has very small diameters and
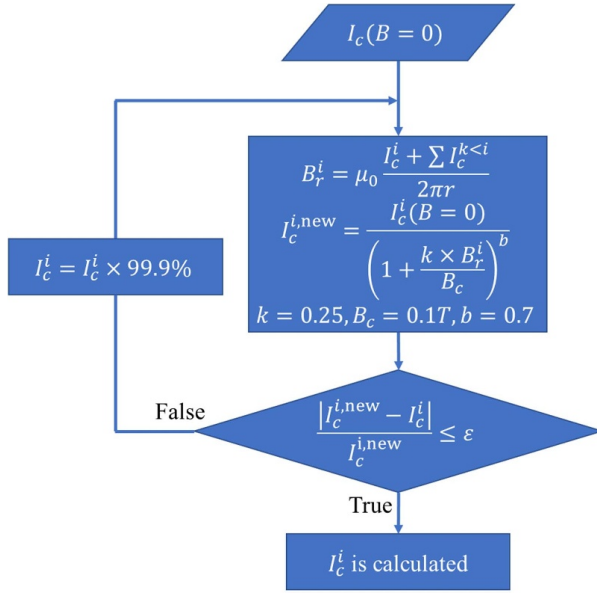
Figure 6. Algorithm to predict critical current of layer *i* of a multilayer CORC® cable.
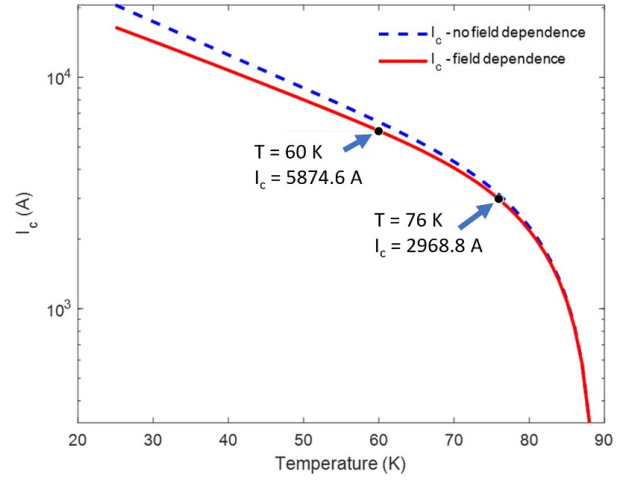

Figure 7. Calculated and measured critical current of REBCO CORC® cable at different temperatures. The $I_c(T)$ curves calculated both with and without considering the $J_c(B)$ were plotted for comparison.

carries large currents at lower operating temperatures, its circumferential magnetic field is considerable. Thus, for better accuracy, the dependence the J_c of HTS tapes on the circumferential magnetic field should be considered in the computations. However, the circumferential magnetic field depends on the cable current. As a result, a numerical procedure is needed.

The circumferential magnetic field applied on an HTS layer depends on its winding radius and the total electrical current running inside that layer. Therefore, the critical current of each HTS layer is calculated and then the summation of the predicted critical current of all HTS layers will provide the critical current of the CORC® cable. As the inner layers can generate a circumferential magnetic field in the outer layers (but not vice versa), the calculation is performed from the innermost layer outward. Figure 6 presents the algorithm used to predict the critical current of layer *i* ($i = 1$–8 with $i = 1$ is the innermost layer) of a CORC® cable at different temperatures. In this case, the I_c of layer k with $k < i$ is already calculated and known. For the initial condition, the I_c of layer *i* is the sum of the critical currents of individual tapes at zero field in that layer, $I_c^i = I_c(B = 0)$. The actual cable I_c must be lower than that initial value due to the magnetic self-field. From that initial value, I_c^i is reduced by 0.1% at each iteration and the circumferential magnetic field B_r^i applying on layer *i* can be calculated from the new values of I_c^i (defined as $I_c^{i,\text{new}}$) and known $I_c^{k<i}$. From the B_r^i, the field-dependent $I_c^{i,\text{new}}(B_r^i)$ is determined based on the Kim model: $I_c^{i,\text{new}}(B_r^i) = I_c(B = 0) / \left(1 + k \times B_r^i / B_c\right)^b$ where the parallel field $B_r^i = \mu_0 \left(I_c^i + \sum I_c^{k<i}\right) / 2\pi r$, $\mu_0 = 4\pi \times 10^{-7}$ H m^{-1} is the free space permeability, *r* is the radius at the current HTS layer, while the parameters $k = 0.25$, $B_c = 0.1$ T and $b = 0.7$ are fitting parameters [20]. The iterative process ends when

the relative difference, $|I_c^{i,\text{new}} - I_c^i| / I_c^{i,\text{new}}$, is lower than a small number epsilon, $\in = 0.005$.

The model was applied to predict the temperature dependence of I_c for the considered CORC® cable with specifications listed in table 1. Figure 7 depicts $I_c(T)$ for the 8-layer CORC® cable with the red solid line representing the values obtained from the numerical method and the blue line representing the values obtained by simply summing the $I_c(T)$ of the individual tapes without considering the effect of the magnetic field on the critical current density. Comparing the two curves in figure 7, the cable critical current calculated without considering the effect of the magnetic field can cause errors of about 10% and 22% at 60 K and 30 K, respectively. The difference between the two curves is more remarkable at lower temperatures because the cable I_c increases at lower temperatures and thus the circumferential magnetic fields impinging on the REBCO tapes are higher and reduce the I_c of the cable more significantly.

The numerical method was validated at 76 K and then used to predict the critical current at lower temperatures. At 76 K, the calculated critical current of the cable is $I_c(76\,\text{K}) \sim$ 2969 A, about 1% higher than the experimental value of $I_c \sim$ 2930 A. In this paper, helium gas at 60 K is considered as the cooling medium for the HTS cable. At this temperature, the cable I_c is predicted to be $I_c(60\,\text{K}) \sim 5875$ A (figure 7), nearly twice that at 76 K, and that value of I_c is used as input for the simulation of the FCL performance in helium gas.

5. Coupled circuit and transverse section models to simulate the FCL performance

Figure 8 presents a flowchart of the numerical simulation conducted to predict the FCL performance and post-fault cooling process of the considered cable (the cable with specification listed in table 1) operating at 60 K in flowing helium gas. The
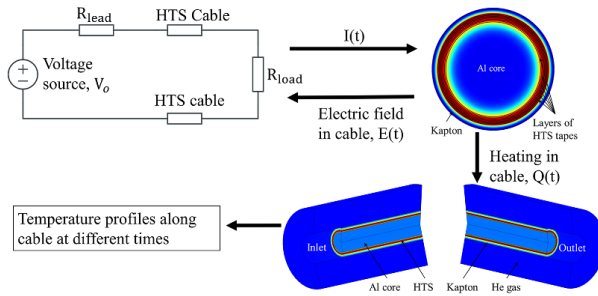
Figure 8. Illustration for numerical approach to simulate the fault current limiting performance and post-fault cooling process for our cable operating at 60 K in flowing helium gas.

study is divided into two stages. In the first stage, a circuit model is coupled with a transverse FEM model to predict the electromagnetic response, temperature rise, and heating generated in the cable during a 40 ms fault. The circuit breaker will open to terminate the fault, turning off the electrical current. The heat generated during the fault is then transferred to the coolant (pressurized helium gas). The second stage of the simulation involves coupled fluid dynamics and heat transfer models to simulate the cooling process along a 50 m-long cable, a length that is realistic for potential use in future electric aircraft.

For the first stage, the coupling between the circuit and the 2D transverse models was achieved by using a method similar to the one reported by Santos *et al* [21]. At each time step, the average electric field over the cross-section of the HTS cable is calculated and used as the driving voltage for the HTS cable components in the circuit model. The purpose of this paper was to demonstrate an approach using coupled circuit model and FEM model to study a fault in a circuit with superconducting cables. In principle, any other electrical components can be added to that circuit and values of electrical components can be changed according to the design of actual electrical systems. Thus, the paper only considered a simplified circuit consisting of the typical components, including the DC power source V_0, the resistance of copper leads R_{lead} and two 50 m-long superconducting cables to transmit the power to the load R_{load}. Values of the components are chosen so that during the normal operating conditions (voltage drop in superconducting cable is zero) the current in the circuit is 4 kA (approximately 68% of the I_c of the cable). During the short-circuit fault ($R_{load} = 0\,\Omega$), the voltage drop in cable can reach 20 V m^{-1} (2000 V for 100 m of HTS cable), as shown in figure 3. Table 2 summarizes the values of the circuit components.

Figure 9 shows plots of the current in the circuit and voltage drop in the HTS cable before, during and after the fault. During normal operation, the HTS cable is in the superconducting state and carries 4 kA. At $t = 8$ ms, the short circuit happens ($R_{load} = 0\,\Omega$), the current quickly surges to approximately 12.2 kA and the electric field in the HTS cable increases from zero to approximately 20 V m^{-1}, as expected. The current is suppressed and gradually decreases to approximately 2 kA at the end of the fault ($t = 40$ ms), enabling the breaker to safely

Table 2. Specification of circuit model.

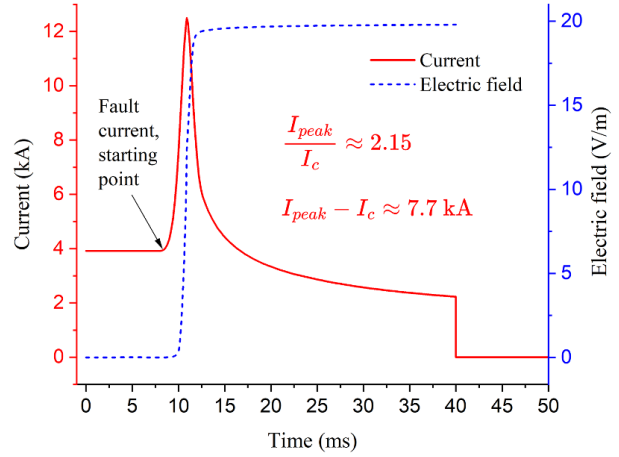|	
Voltage source, V_0 (V)	2000
Load resistance, R_{load} (Ω)	0.5
Lead resistance, R_{lead} (Ω)	0.01
Total HTS cable length, L (m)	100
Voltage source, V_0 (V)	2000
Load resistance, R_{load} (Ω)	0.5
Lead resistance, R_{lead} (Ω)	0.01
Total HTS cable length, L (m)	100

Figure 9. Current in the circuit and electric field in the HTS cable before, during and after the fault.

open the circuit. Without the presence of an HTS cable, the fault current will be $I_{fault} = V_0/R_{lead} = 200$ kA. Thus, the HTS cable significantly suppresses the fault current from 200 kA to the peak current of 12.2 kA, enabling the safe operation of the breakers and preventing catastrophic damage to the electrical components and systems. It is worth noting that the same cable can handle a much higher current above its I_c when it operates at lower temperatures due to the significant reduction of the resistivity of the copper stabilizer at lower temperature. To produce about the same voltage drop of 20 V m^{-1}, our sample cable can handle $\Delta I \sim 3$ kA above its I_c at $T = 76$ K and handle $\Delta I \sim 7.7$ kA above the I_c at $T = 60$ K.

Figure 10 shows power losses (in W/m) generated in different layers of the cable during the fault. At the beginning of the fault, the current penetrates from the outer layers inward due to the skin effect [13]. Consequently, the power losses are higher in the outer layers, as expected. When the fault current reaches and goes beyond the I_c of the cable, the current is distributed more evenly between the layers and the heating is nearly the same in all the layers. The slight variation of heating in the layers later during the fault is caused by the differences in the temperature rise in those layers. As mentioned, previously the power losses calculated in this first simulation stage are used as input for the second stage to simulate the cooling process after the fault is cleared.

Figure 11 depicts the temperature rise in the HTS layers during the fault. The temperature increase tends to be higher
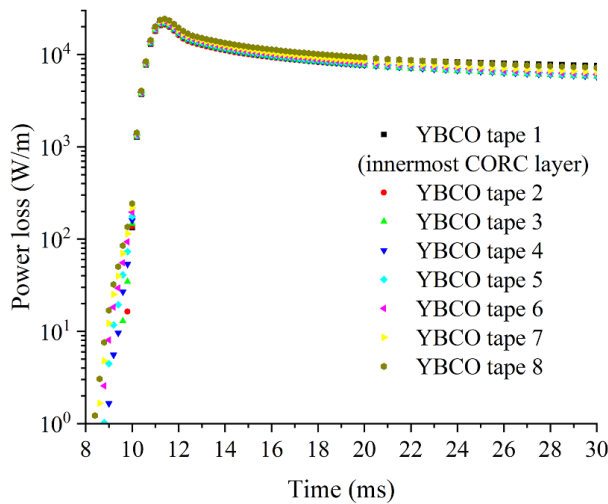
Figure 10. Power loss at different HTS layers calculated by the 2D transverse model.
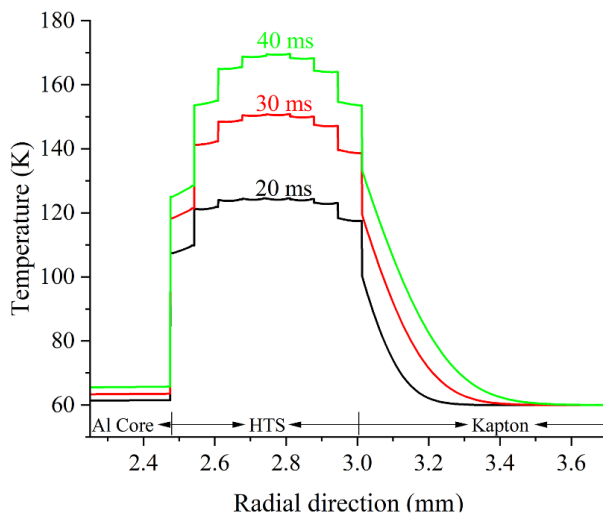

Figure 11. Temperature profile along the radius direction at different times during the fault.

in the middle layers because the heat in the outer and inner layers can be transferred out faster. The large step between the temperatures in the aluminum core and the HTS winding is caused by thermal insulation of the polyester layer covering the core, which is used as the electrical insulation. Due to the thermal contact resistance between HTS layers, the temperature profiles inside the HTS winding region have staircase shapes. Without taking the thermal contact resistance into account, the temperature profiles are much smoother (see figure 4(b) or [13]). This difference indicates an important role of the thermal contact resistance in the heat transfer process. As seen in figure 11, the maximum temperature in the cable winding reaches 165 K at the end of the fault ($t = 40$ ms). The temperature in the aluminum core increases from 60 K

to approximately 66 K. At the end of the fault, the temperature near the outside surface of the Kapton overwrap is still at 60 K, indicating that heat is still trapped inside the cable during the 40 ms fault and there is no heat transferred to the helium gas. Therefore, the 2D transverse model used to simulate the FCL performance does not need to account for the heat transfer from inside the cable to the helium coolant during the 40 ms fault. The heat generated inside the cable will remain uniform along its length during this time, as no heat is transferred to the helium gas coolant. As a result, the 2D transverse model can calculate the heating power within the cable and transfer this heating power to the longitudinal 2D model for further cooling simulations. This approach is both accurate and significantly reduces computational time and complexity.

6. Longitudinal 2D model for long-length cable cooled by helium gas

Each long cable can be cooled with multiple cooling loops for a more uniform operating temperature and faster cooling process. A simplified cooling apparatus with multiple cooling loops for a 50 m-long cable is shown in figure 12. The considered cable (not depicted in the figure) is placed inside a cryostat, which is cooled with flowing helium gas that enters through inlets and returns via three outlets positioned alternately between the inlets, as illustrated in figure 12. The flow directions of the helium gas are indicated by green arrows. Each inlet and outlet is equipped with a control valve that can be adjusted to optimize the flow rates in different sections. Sections with current leads, which may have higher heat leakage, will require more cooling power. For the 50 m-long cable, each section between adjacent inlet and outlet is 10 m long. Therefore, this paper focuses on a numerical model to simulate the cooling process for a 10 m-long section cooled with pressurized, flowing helium gas. The model was performed in the longitudinal cross-section of the 10 m system, with the CORC® cable positioned at the center of the cryostat and cold helium gas flowing from one end (inlet) to the other (outlet). To have a stable, uniform temperature of 60 K along the 10 m-long cable as assumed in the 2D transverse model, the jacket of the cryostat is assumed to have perfect thermal insulation (perfect thermal insulation boundary). This simulation focuses on solving the multi-scale challenge to study the heat transfer from the cable to the coolant and the impact of coolant flow rate on the cooling processes. The simulations must be performed on an entire 10 m-long cable and simultaneously cope with many thin constituent layers of REBCO tapes with thicknesses at the micrometer scale. Two simple approaches were used to resolve this multi-scale challenge and reduce the computation time with acceptable error. First, each REBCO tape with several thin layers of different materials can be treated as a single domain of homogeneous material of equivalent thermal properties. The equivalent specific heat and mass density are calculated as the average heat capacity and mass density of the constituent layers. These constituent layers are connected in series in the heat transfer path, so the equivalent thermal conductivity can be calculated easily from
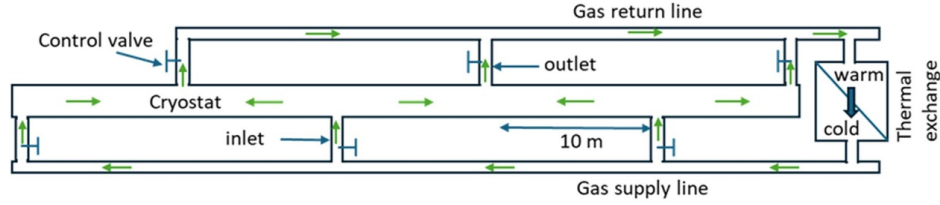
Figure 12. Simplified cooling apparatus for a 50 m long cable with a multiple-cooling-loop cryostat.

the thickness and thermal conductivities of constituent layers [22]. Secondly, mapped meshes were used to reduce the number of nodes and to ensure the simulation runs are stable given the high aspect ratio of the mapped meshes. It is worth noting that the thermal contact resistance $R_s = 9 \times 10^{-5}$ K m^2 W^{-1} between HTS layers was also considered in this longitudinal model.

Coupled laminar fluid dynamics and heat transfer models built in the commercial COMSOL^{TM} Multiphysics package were used to simulate the cooling process of the cable placed in the center of a cryostat with a laminar flow of helium gas. The temperature and velocity of the helium gas are set as constant inputs at the inlet boundary for both heat transfer and laminar fluid dynamic models. The laminar flow of helium gas inside the cryostat is simply governed by the mass conservation equation [23]:

$$\frac{\partial \rho_p(T)}{\partial t} + \nabla.(\rho_p(T)\boldsymbol{u}) = 0 \tag{5}$$

where $\rho_p(T)$ is the density of the helium gas at pressure of 20 atm and $\boldsymbol{u}$ is the velocity vector of the gas flow. We assume that the flow of helium gas in the cryostat is well regulated by control valves at the inlets and outlets so that the change in the pressure of the helium gas in the system is negligibly small during the fault. Thus, the heat transfer in the cryostat is described by [23]:

$$\rho_p(T) C_p(T) \left(\frac{\partial T}{\partial t} + \boldsymbol{u}\nabla T\right) + \nabla.q = \boldsymbol{Q}. \tag{6}$$

In equation (6), $C_p(T)$ is the specific heat of materials. For solid materials (such as HTS tapes and insulations), $\boldsymbol{u}$ will be zero. For helium gas, velocity vector $\boldsymbol{u}$ calculated from laminar fluid dynamics models will be used as input for equation (6). The heat flux vector q in equation (6) is calculated from the thermal conductivity k and gradient of the temperature as follows:

$$q = -k\nabla T. \tag{7}$$

The heating power calculated by the 2D traverse model and shown in figure 10 will be used as input for the heating source Q in equation (6). More details of the governing equations for these models can be found in the COMSOL^{TM} Multiphysics package [23]. The parameters for the helium cryostat and the simulation parameters for the 2D longitudinal model are given in table 3. The pressure of the inlet is assumed to be 20 atm and the pressure inside the 10 m long section is slightly varied

Table 3. Parameters of cooling system and simulation parameters for the longitudinal 2D model.

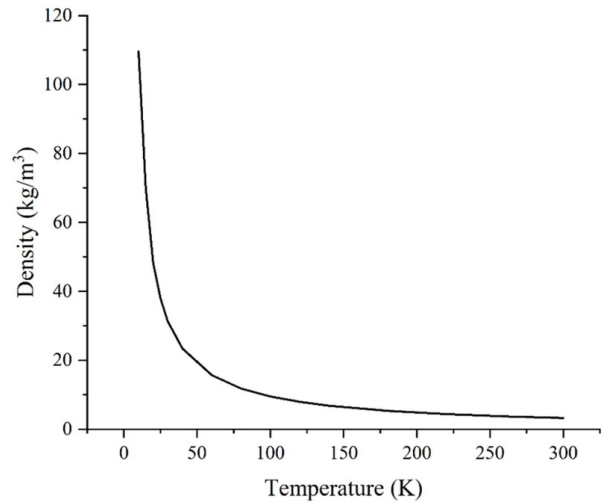|	
Radius of cryostat (m)	0.01
Length of cryostat (m)	10
Velocity of helium gas, v_{He} (g/s)	2.5, 5 and 10
Pressure (atm)	20
Viscosity of helium gas, μ (Pa.s)	0.00006
Number of quadrilateral elements	160 080
Number of elements along cable	1000
Number of degrees of freedom	294 622

Figure 13. Density of helium gas with respect to temperature at pressure 20 atm.

along 10 m long cryostat. However, that pressure variation is small enough to approximately use the temperature dependences of density, heat capacity and thermal conductivity of helium gas at a constant pressure of 20 atm for the entire simulation process. These temperature dependences are plotted in figures 13–15, respectively [24].

Figure 16 depicts the temperature distribution over the cross-section of the cooling system near the inlet and outlet locations at 0.1 s and at 1 s when the helium gas flows at the rate of 5 g s^{-1}. For more details, temperature profiles along the radius direction at different times, $t = 0.04$ s, 0.1 s, 1 s and 5 s were plotted in figure 17 for both the inlet and outlet locations. Because the thermal contact resistance between HTS layers was considered in the 2D longitudinal mode, the
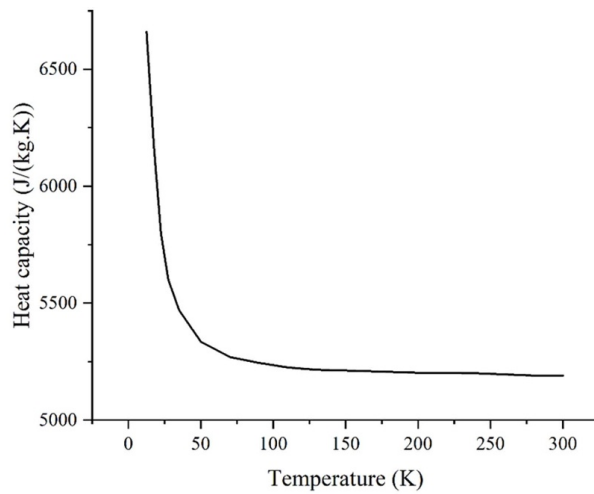
Figure 14. Heat capacity of helium gas with respect to temperature at pressure 20 atm.
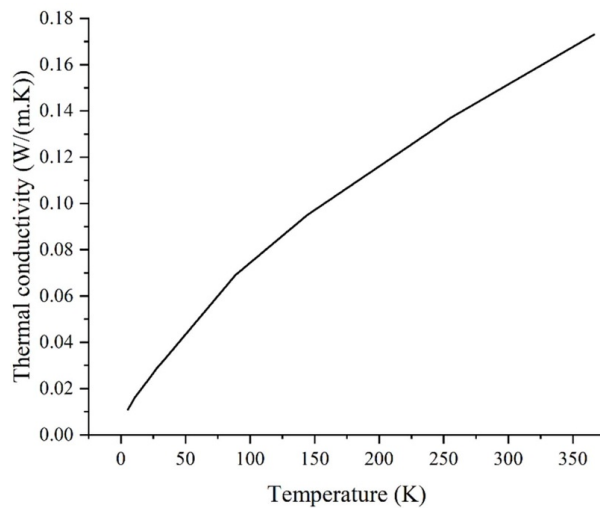

Figure 15. Thermal conductivity of helium gas with respect to temperature at pressure 20 atm.

Figure 16. Comparison temperature distribution between inlet (left) and outlet (right) of the cable at 0.1 s (top) and 1 s (bottom).

Figure 17. Temperature along the radial direction at the inlet and outlet locations and at different times.

temperature profiles also have staircase shapes, similar to that shown in figure 11 which was obtained by the 2D transverse model. As expected, the temperature profile along the cable radius at $t = 0.04$ s shown in figure 17 (obtained with 2D longitudinal model) reproduces well that which is shown in figure 11 (obtained with the 2D transverse model), confirming the validity of the longitudinal model.

As seen in figure 17, even at $t = 0.1$ s (or 0.06 s after the fault ends at $t = 0.04$ s), the temperature distribution along the radius direction at the inlet and outlet locations are identical. This means that the heat generated in the winding has not been transferred out to the coolant at that time. At later times, such
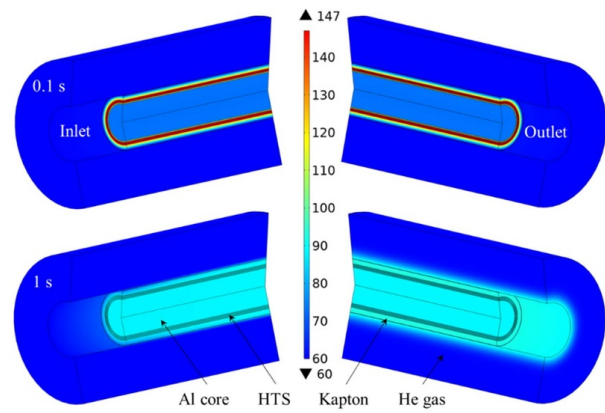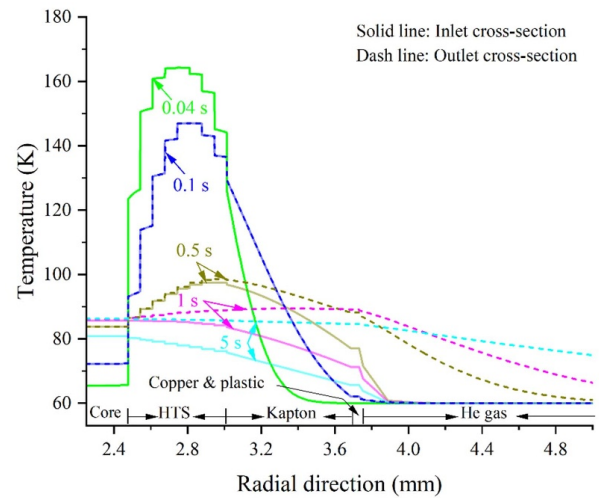
as $t = 1$ s or 5 s, the temperature at the inlet location is considerably lower than that at the outlet. This is understandable because the cable at the inlet location will be cooled down faster by colder helium gas.

The temperature profiles along the 10 m-long cable in the innermost and outermost REBCO tapes at different times up to 500 s after the fault are plotted in figures 18 and 19, respectively. Since the thermal conductivity of the Kapton insulation is significantly higher than that of REBCO winding, the difference in the cooling rate for the outermost and innermost layers is insignificant. Overall, the temperatures in these innermost and outermost layers gradually increase during and right after the fault. This means that the heat generated in HTS layers is trapped at the boundary of the winding due to thick insulation. The temperatures of the innermost and outermost layers reach
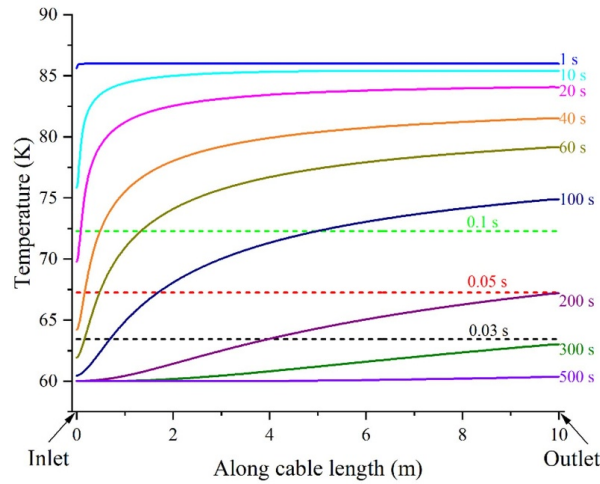
Figure 18. Temperature distribution along the cable length for the innermost REBCO layer at different times.
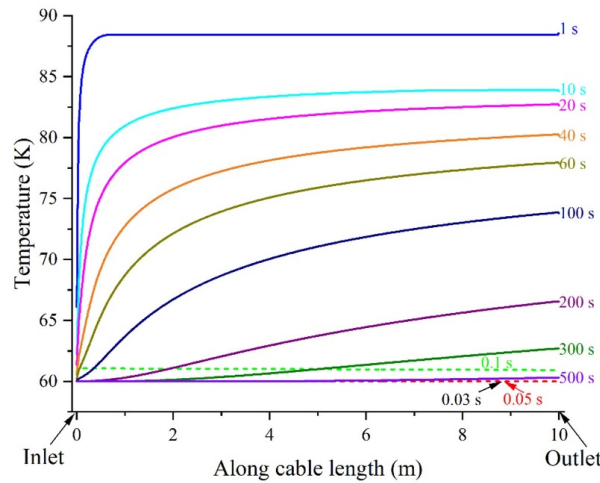

Figure 19. Temperature distribution along the cable length for the outermost REBCO layer at different times.

peaks of nearly 90 K at approximately 1 s then start decreasing. As expected, the cable at the inlet location is cooled down quickly and the cooling rate gradually reduces toward the outlet. The temperature of the cable at the inlet location decreases to nearly 60 K, the original temperature, after about 100 s. However, it takes approximately 500 s for the cable at the outlet location to be cooled back to that temperature. Figure 20 depicts the impact of the flow rate v_{He} of the helium gas, on the cooling rate for the innermost layer at the inlet and outlet locations. It is obvious that the inlet location is cooled much faster than the outlet location and the cable are cooled down faster with higher v_{He}. With $v_{He} = 10\,\mathrm{g\,s^{-1}}$, it takes approximately 100 s and 400 s to cool the innermost cable layer at the inlet and outlet back to nearly 60 K, respectively. In case of
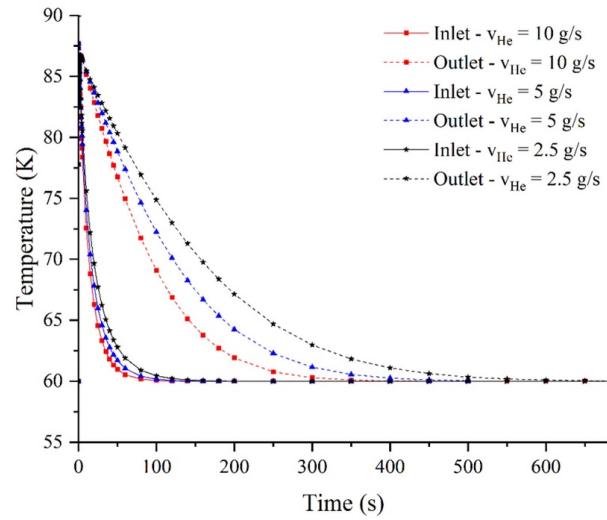

Figure 20. Evolution of temperature of the innermost layer at the inlet and outlet locations for different helium gas flow rates.

$v_{He} = 2.5\,\mathrm{g\,s^{-1}}$, it takes approximately 200 s and 660 s for the cable to be cooled back to nearly 60 K at the inlet and outlet locations, respectively.

7. Conclusion and outlook

The accuracy of our coupled electromagnetic-thermal 2D transverse model for simulating the FCL performance of CORC® cable was significantly improved by more accurately estimating the thicknesses of the Cu and Ag layers and considering the thermal contact resistance between the HTS tapes. This refined model reproduces the experimental data very well for a long duration fault. To accurately predict the fault current limitation in HTS cables at temperatures less than 70 K, accurate prediction of the dependence of the cable's critical current on temperature is essential. A numerical method was developed to determine the critical current of CORC® cables for a wide range of temperatures based on the $I_c(T, B)$ of single tapes. The model is suitable for cables with an arbitrary number of layers and HTS tapes per layer. The model generated the I_c at 76 K for an 8-layer cable with a 1.4% discrepancy with respect to the experimental data. The model developed was then used to predict I_c of the cable at 60 K, the operating temperature of the cable in He gas.

The performance of the FCL and the cooling behavior of an 8-layer HTS cable cooled by helium gas were thoroughly investigated using FEM simulations conducted in two stages. In the first stage, a circuit model was coupled with a refined two-dimensional transverse model to simulate the FCL performance of the cable. The quick superconducting-to-normal transition of the HTS cable suppressed the fault current to about 12.2 kA (210% of cable I_c) which is substantially lower than the fault current in the system without

an HTS cable. The 40 ms fault at voltage drop of 20 V m^{-1} along the cable resulted in temperature rise to about 165 K. The heating power calculated in the first stage was used as the input for the longitudinal 2D simulations which use coupled lamina fluid dynamics and heat transfer models to address the multi-scale challenge of studying heat transfer from the cable to the coolant and the impact of coolant flow rate on the cooling processes for a long-length cable. The simulation indicated that it takes about 500 s to cool down a 10 m long cable to its original operating temperature of 60 K if helium gas at 20 atm pressure and a mass flow rate of 5 g s^{-1} is used as the coolant.

While the 2D transverse model has been well validated against experiments at liquid nitrogen temperature, it would be interesting to build a 10 m long cooling system using helium gas in the future to test the FCL performance at lower temperatures and validate/refine the longitudinal model. A validated longitudinal model would be a useful tool in the design and optimization of cooling systems for HTS FCL cables. Additionally, there would be heat leaks through the cryostat and current leads at the terminals, causing non-uniform temperatures along the cable. The heat leak depends on the design of the cryostat and current leads. If those heat leak parameters are known, it would be straightforward to consider these heat leaks in the longitudinal models.

Data availability statement

Acknowledgments

ORCID iDs

Linh Ngoc Nguyen ⓘ https://orcid.org/0000-0002-9108-0581
Jeremy Weiss ⓘ https://orcid.org/0000-0003-0026-3049
Francesco Grilli ⓘ https://orcid.org/0000-0003-0108-7235
Danko van der Laan ⓘ https://orcid.org/0000-0001-5889-3751
Doan Ngoc Nguyen ⓘ https://orcid.org/0000-0003-2605-1829

References

[1] Stemmle M, Merschel F, Noe M and Hobl A 2013 Ampacity project-Worldwide first superconducting cable and fault current limiter installation in a German city center *22nd Int. Conf. and Exhibition on Electricity Distribution (CIRED 2013)* pp 1–4

[2] Marchionini B G, Yamada Y, Martini L and Ohsaki H 2017 High-temperature superconductivity: a roadmap for electric power sector applications, 2015–2030 *IEEE Trans. Appl. Supercond.* **27** 1–7

[3] Malozemoff A P, Yuan J and Rey C M 2015 High-temperature superconducting (HTS) AC cables for power grid applications *Superconductors in the Power Grid* (Woodhead Publishing) pp 133–88

[4] Schmidt W, Kraemer H-P, Neumueller H-W, Schoop U, Verebelyi D and Malozemoff A P 2007 Investigation of YBCO coated conductors for fault current limiter applications *IEEE Trans. Appl. Supercond.* **17** 3471–4

[5] Yazdani-Asrami M, Seyyedbarzegar S, Sadeghi A, de Sousa W T and Kottonau D 2022 High temperature superconducting cables and their performance against short circuit faults: current development, challenges, solutions, and future trends *Supercond. Sci. Technol.* **35** 083002

[6] van der Laan D C, Weiss J D, Kim C H, Graber L and Pamidi S 2018 Development of CORC® cables for helium gas cooled power transmission and fault current limiting applications *Supercond. Sci. Technol.* **31** 085011

[7] Du H I, Kim T M, Han B S and Hong G H 2015 Study on verification for the realizing possibility of the fault-current-limiting-type HTS cable using resistance relation with cable former and superconducting wire *IEEE Trans. Appl. Supercond.* **25** 1–5

[8] Tomita M, Muralidhar M, Suzuki K, Fukumoto Y, Ishihara A, Akasaka T and Kobayashi Y 2013 Design and construction of a high temperature superconducting power cable cryostat for use in railway system applications *Supercond. Sci. Technol.* **26** 105005

[9] Zajaczkowski B, Giesbers A J M, Holtrust M, Haenen E and Den Heijer R 2011 Feasibility of inline cooling in long distance HTS power line *Cryogenics* **51** 180–6

[10] Fan Y F, Gong L H, Xu X D, Li L F, Zhang L and Xiao L Y 2005 Cryogenic system with the sub-cooled liquid nitrogen for cooling HTS power cable *Cryogenics* **45** 272–6

[11] Pamidi S, Kim C H, Kim J-H, Crook D and Dale S 2012 Cryogenic helium gas circulation system for advanced characterization of superconducting cables and other devices *Cryogenics* **52** 315–20

[12] Fitzpatrick B K, Kephartl J T and Golda E M 2007 Characterization of gaseous helium flow cryogen in a flexible cryostat for naval applications of high temperature superconductors *IEEE Trans. Appl. Supercond.* **17** 1752–5

[13] Nguyen L N, Naud M, Weiss J, Pamidi S, Dönges S A, van der Laan D and Nguyen D N 2022 Simulation for the fault current limiting operation of REBCO CORC® superconducting cables with different core materials *IEEE Trans. Appl. Supercond.* **33** 1–8

[14] Grilli F, Pardo E, Stenvall A, Nguyen D N, Yuan W and Gömöry F 2014 Computation of losses in HTS under the action of varying magnetic fields and currents *IEEE Trans. Appl. Supercond.* **24** 78–110

[15] Pi W, Liu Z, Li G, Ma S, Meng Y, Shi Q, Dong J and Wang Y 2020 4D simulation of quench behavior in quasi-isotropic superconducting cable of stacked REBCO tapes considering thermal contact resistance *Supercond. Sci. Technol.* **33** 084005

[16] Xue S, Sumption M D, Panik D, Thong C J, Guo X, Majoros M and Collings E W 2022 Electrical contact resistance in REBCO stacks and cables with modified surfaces *IEEE Trans. Appl. Supercond.* **32** 4802506

[17] Prasher R S and Phelan P E 2006 Microscopic and macroscopic thermal contact resistances of pressed mechanical contacts *J. Appl. Phys.* **100** 063538

[18] Dhuley R C 2019 Pressed copper and gold-plated copper contacts at low temperatures–A review of thermal contact resistance *Cryogenics* **101** 111–24

[19] Wimbush S, Strickland N and Pantoja A 2016 A high-temperature superconducting (HTS) wire critical current database *figshare. Collection.* (https://doi.org/10.6084/m9.figshare.c.2861821.v18)

[20] Yang J, Li C, Tian M, Liu S, Shen B, Hao L, Ozturk Y and Coombs T 2022 Analysis of AC transport loss in conductor on round core cables *J. Supercond. Novel Magn.* **35** 1–7

[21] Santos B M O, Dos Santos G, Sirois F, Brambilla R, de Andrade Junior R, Sass F and Grilli F 2022 2D modeling of HTS coils with T-A formulation: how to handle different coupling scenarios *IEEE Trans. Appl. Supercond.* **32** 1–4

[22] Yuan W-B, Yu N, Li L-Y and Fang Y 2022 Heat transfer analysis in multi-layered materials with interfacial thermal resistance *Compos. Struct.* **293** 115728

[23] (Available at: www.comsol.com)

[24] Mc Carty R D 1973 Thermodynamic properties of helium 4 from 2 to 1500 K at pressures to 108 Pa *J. Phys. Chem. Ref. Data* **2** 92a3–1042